Research paper

Toward noble-metal-free visible-light-driven photocatalytic hydrogen evolution: Monodisperse sub–15 nm Ni_2P nanoparticles anchored on porous g-C_3N_4 nanosheets to engineer 0D-2D heterojunction interfaces

Deqian Zeng[a,b], Wanjie Xu[a], Wee-Jun Ong[b,*], Juan Xu[c], He Ren[c], Yuanzhi Chen[a,*], Hongfei Zheng[a], Dong-Liang Peng[a,*]

[a] Department of Materials Science and Engineering, Collaborative Innovation Center of Chemistry for Energy Materials, College of Materials, Xiamen University, Xiamen, 361005, China
[b] Institute of Materials Research and Engineering (IMRE), Agency for Science, Technology and Research (A*STAR), 2 Fusionopolis Way, Innovis, Singapore, 138634, Singapore
[c] State Key Laboratory of Physical Chemistry of Solid Surfaces and Department of Chemistry, College of Chemistry and Chemical Engineering, Xiamen University, Xiamen, 361005, China

ARTICLE INFO

ABSTRACT

Exploring robust and low-cost noble-metal-free co-catalysts to substitute precious noble-metal is of great importance in both fundamental research and practical applications. Herein, we employ a novel solution-phase method to synthesize highly monodisperse zero-dimensional (0D) nickel phosphide (Ni_2P) nanoparticles, which were then anchored on two-dimensional (2D) porous g-C_3N_4 nanosheets *via* a facile self-assembly route to develop the intimate 0D-2D heterojunction interface. The outstanding feature of the material is that the resultant hybrid nanocomposite exemplified efficient noble-metal-free photocatalytic H_2 production under visible light. Under optimal conditions, the Ni_2P embedding was found to be 3.5 wt%, giving a remarkable H_2 production rate of 474.7 $\mu mol\, g^{-1}\, h^{-1}$ and an apparent quantum yield (AQY) of 3.2% at 435 nm, surpassing most of the reported noble-metal-free co-catalysts-modified g-C_3N_4 photocatalysts. The superior photoactivity of the hybrid nanostructure is attributed to the profound role of Ni_2P as an excellent reduction co-catalyst to hamper the recombination of charge carriers from g-C_3N_4 and also provide good electrical conductivity, which could be substantiated by photoelectrochemical (PEC) experiments, photoluminescence (PL) spectra, and electron paramagnetic resonance (EPR) spectroscopic studies. Benefitting from the intriguing properties of Ni_2P and g-C_3N_4, this work presents a new platform to uncover the immense potential of noble-metal-free nanomaterials as the next generation photocatalysts in multifunctional application prospects not only in the water splitting reaction, but also in other energy-related fields such as CO_2 reduction and solar cells. It is also anticipated that the solution-phase hybridization technique could be extended to synergistically integrate g-C_3N_4 with a myriad of nanocrystals for multitudinous chemical reactions.

1. Introduction

As a low-cost renewable carbon-free energy source, solar light can be harvested and converted into highly energetic sustainable fuels in chemical bonds such as hydrogen (H_2) without any carbon footprint with the aid of appropriate catalysts. At present, photocatalytic production of H_2, which is one of the Holy Grails of chemistry, has been widely reported as an attractive and sustainable approach for effective utilization of clean and inexhaustible solar energy, by itself, will simultaneously circumvent the global energy and environmental problems caused by the rampant consumption of fossil fuels [1,2].

Recently, as a metal-free polymeric-like semiconductor photocatalyst, graphitic carbon nitride (g-C_3N_4) has enthralled enormous attention in the realm of energy production due to its suitable band gap positions for photocatalytic water splitting, high chemical- and photo-stability [3–9]. However, the high recombination rate of photo-excited carriers significantly limits the photocatalytic H_2 evolution activity of the single-component g-C_3N_4 photocatalyst [10–14]. Hitherto, unremitting efforts have been devoted to designing and engineering co-catalysts-modified g-C_3N_4 as an auspicious and fascinating solution to ameliorate its photoactivity towards H_2 evolution [15,16]. The co-catalysts play an indispensable role in extracting photo-generated charge carriers,

hosting reaction active sites, and reducing the reaction energy barriers for photocatalytic H_2 generation [15,17]. Undeniably, noble metals such as Pt are commonly utilized as efficient co-catalysts for improving photocatalytic H_2 evolution of g-C_3N_4 based on the previous studies [18–23]. However, the scarcity and extremely high-cost of noble metals widely impede their practical use in the hydrogen production at a large scale. Therefore, daunting challenges still exist in constructing g-C_3N_4 hybrid systems, which comprise relatively less expensive and earth-abundant co-catalysts for remarkable photocatalytic water splitting.

In the last several years, noble-metal-free co-catalysts such as MoS_2 [24,25], WS_2 [26], NiS, [27,28], $Ni(OH)_2$ [29], and Ni nanoparticles [17,30,31] decorated onto g-C_3N_4 have underpinned a renaissance of surging interest stemming from their extraordinary H_2 evolution photoactivity. In contrast with the aforementioned co-catalysts, transition metal phosphides (*e.g.*, Ni_2P, Co_2P, FeP, *etc.*) as co-catalysts modified g-C_3N_4 systems are relatively seldom reported in the literature and thus worthy of extensive research. As a proof of concept, transition metal phosphides have been employed as highly active non-noble-metal electrocatalysts in electrochemical hydrogen generation [32,33], and also as efficient co-catalysts for photocatalytic and photoelectrochemical H_2 generation, which ensued from their approximate zero-valent metallic properties and long-term stability [34]. For example, Ni_2P [35,36], MoP [37], and Co_xP [38] can all act as efficient co-catalysts integrated CdS nanorods and highly improve the performance for photogeneration of hydrogen in water. Additionally, CoP, Ni_2P and Cu_3P that were produced by thermal reduction of hypophosphite and supported on hexagonal CdS has also been used as efficient heterojunction nanocomposites for hydrogen evolution under solar irradiation [39]. To the best of our knowledge, only a few reports have demonstrated the use of transition metal phosphides as co-catalysts incorporated with g-C_3N_4 for the photocatalytic hydrogen evolution reaction since 2016, namely CoP [40–42], $Ni_{12}P_5$ [43], and Ni_2P nanoparticles [44–47]. Nevertheless, the preparation and hybridization of metal phosphides with the aim of attaining simultaneously pure phase, well-crystallized, and monodisperse nanosized particles remain an onerous task to be achieved in the g-C_3N_4 nanohybrid systems. Notably, it has become a stumbling block and a burgeoning challenge to develop a facile and convenient strategy to couple metal phosphides with g-C_3N_4 nanosheets for the intimate connection and tight heterojunction for boosted photocatalytic performance.

Thus far, the gas-solid reaction strategy with both NaH_2PO_2 and $NH_4H_2PO_4$ as P sources is widely utilized, but the decomposition of hypophosphites releasing PH_3 necessitates high temperature and multiple steps to achieve metal phosphides [34]. Furthermore, conventional mechanical blending or suspension solvent stirring method for the loading of co-catalysts on g-C_3N_4 would cause the irregularly-distributed load or particle shedding during the catalytic reaction, which leads to markedly reduced photocatalytic performance. At this juncture, the synthesis of pure phase and monodisperse metal phosphides remains a scientifically arduous task as a result of their various multifarious phases and uncontrolled morphology. Considering the rapidly-blossoming progress in the solution-phase synthesis of metal phosphides, it is envisioned that an efficient strategy in anchoring g-C_3N_4 with metal phosphides through a solution-phase method is of utmost significance for the formation of well-contacted heterojunction nanostructures between g-C_3N_4 and metal phosphides. Therefore, the preparation of metal phosphide nanoparticles with pure phase, well-crystallized and narrow particle size distribution *via* a solution-phase method should be further examined. Compared to the conventional gas-solid reaction strategy which requires multiple steps, high temperature and the release of highly toxic gas (PH_3) for the development of g-C_3N_4/metal phosphide, the hybridization technique of 0D monodisperse metal phosphide nanoparticles and 2D g-C_3N_4 nanosheets through a solution-phase self-assembly approach at room temperature warrants a special level of merits for further scrutiny.

In view of the above-mentioned Achilles' heels, we present a facile solution-phase self-assembly route to incorporate two-dimensional (2D) porous g-C_3N_4 nanosheets and zero-dimensional (0D) nanocrystalline Ni_2P co-catalysts, in which the monodisperse Ni_2P nanoparticles are pure phase, well-crystallized and endow narrow particle size distribution of 10.3 nm in average synthesized by the phosphorization of intermediate monodisperse Ni. The as-prepared Ni_2P nanoparticles were then tightly anchored on the porous g-C_3N_4 nanosheets through continuous ultrasonication in the mixture of DMF/hexane solution. Interestingly, the as-obtained g-C_3N_4/Ni_2P heterojunction nanocomposites exhibit conspicuously enhanced hydrogen evolution under visible light radiation even in the absence of noble metals. To this end, it is expected that our study will eminently contribute to a new research paradigm for the rational development of cost-effective, high-efficient, and environmental friendly hybrid heterojunction nanocomposites for sustainable solar energy production.

2. Results and discussion

Herein, we present a novel two-step synthetic route to synthesize Ni_2P in the oleylamine (OAm) system, and also to introduce a new optimization technique incorporating Ni_2P nanoparticles into porous g-C_3N_4 nanosheets. Fig. 1a illustrates an optimized synthetic strategy for fabrication of Ni_2P nanoparticles, which includes the preparation of intermediate monodisperse Ni nanoparticles, and the formation and growth of Ni_2P by using tri-*n*-octylphosphine (TOP) as a phosphorus source heated at a higher temperature. More specifically, firstly,
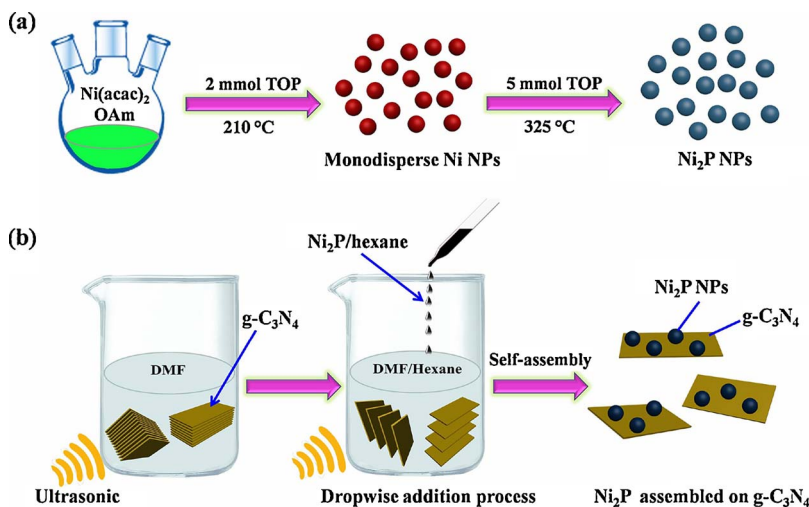

Fig. 1. (a) Schematic synthesis of Ni_2P nanoparticles. (b) Schematic of 0D Ni_2P nanoparticles assembled on the 2D g-C_3N_4 nanosheets.

monodisperse Ni nanoparticles (Fig. S1) were successfully synthesized *via* thermal decomposition of nickel acetylacetonate in the presence of OAm at a relatively low temperature of 210 °C using less TOP according to our previous report [48]. Subsequently, the intermediate Ni can be *in situ* phosphorized using excess TOP at an elevated temperature of 325 °C. Such solution-phase synthesis process efficiently facilitates pure phase Ni_2P, leading to the fabrication of narrow size distribution of nanoparticles. Inspired by the previous reports on the design of the graphene-supported monodisperse nanoparticles by means of sonicating the mixed solvents [49,50], it is envisaged that such process can also be applied to the $g-C_3N_4$-based hybrids due to its sheet-like structure akin to graphene. Fig. 1b reveals a direct solution-phase self-assembly method to deposit Ni_2P nanoparticles on the $g-C_3N_4$ nanosheets through sonicating the mixture of the Ni_2P/hexane and $g-C_3N_4$/DMF solution. First, bulk $g-C_3N_4$ is exfoliated into sheet structures *via* an ultrasonic method in DMF solvent. Second, the Ni_2P nanoparticles dispersed in hexane was added dropwise into the $g-C_3N_4$ suspension under continuous sonication. The Ni_2P nanoparticles will be spontaneously assembled on the porous $g-C_3N_4$ sheets to achieve a minimum surface energy, which can be attributed to the absorption and interaction of functional groups and also can be trapped by the multiple pores on $g-C_3N_4$. As shown in Fig. S2, we can evidently observe the direct assembly of Ni_2P nanoparticles on the $g-C_3N_4$ surface by mixing the hexane dispersion of Ni_2P and the DMF solution of $g-C_3N_4$ sheets under sonication. Therefore, the sonication and aging process in toluene lead to intimate interfacial contact between porous $g-C_3N_4$ and Ni_2P. The adsorbed Ni_2P nanoparticles on the surface of $g-C_3N_4$ could be intercalated and embedded into the $g-C_3N_4$ layers through sonication and sedimentation. As such, the solution-phase hybrid process plays a central role in constructing tight heterojunction interfaces between porous $g-C_3N_4$ and Ni_2P while maintaining the desired size and morphology of Ni_2P and $g-C_3N_4$.

Fig. 2a shows the transmission electron microscopy (TEM) images of the $g-C_3N_4$, indicating the typical 2D nanosheet and porous structures of the as-prepared $g-C_3N_4$. As shown in Fig. 2b, the low-magnification TEM image of Ni_2P nanoparticles reveals the narrow particle size distribution and highly uniform dispersion. The average size of Ni_2P was determined as 10.3 nm (Fig. S3). The corresponding selected area electron diffraction (SAED) pattern (Fig. S4) shows diffraction rings which are referenced to the (111), (201), (210) and (300) planes of hexagonal lattice structure of Ni_2P, as well as implying the high crystallinity of Ni_2P nanoparticles. Fig. 2c and d show the low-magnification and high-magnification TEM images of $g-C_3N_4$/10% Ni_2P obtained from the *ex-situ* solution-phase hybrid process *via* sonication. It is apparent that the Ni_2P nanoparticles were uniformly deposited and tightly anchored on the $g-C_3N_4$ nanosheets without severe agglomeration. As depicted in Fig. S5, when the loading amount of Ni_2P increased, a large quantity of Ni_2P nanoparticles was anchored on the $g-C_3N_4$, highlighting that each component in the hybrid system should be precisely controlled during the solution-phase process.

The TEM images (Fig. 3a and b) exemplified that Ni_2P nanoparticles were uniformly embedded into the $g-C_3N_4$ sheets-layers, and fascinatingly, parts of the pores in $g-C_3N_4$ have been occupied by the Ni_2P nanoparticles. The HRTEM image taken from an individual nanocrystal (upper inset in Fig. 3b) exhibits a lattice fringe of 0.223 nm, corresponding to the (111) planes of hexagonal Ni_2P (JCPDS#74–1385). Fig. 3c shows the high-angle annular dark-field (HAADF) image of the hybrid photocatalysts. The Ni_2P nanoparticles exhibit a much brighter contrast than the $g-C_3N_4$ nanosheets matrix due to the stronger ability to scatter electrons as compared to $g-C_3N_4$ which has a lower average atomic number. Elemental maps (Fig. 3d–g) obtained in the STEM mode confirm the presence of constituent carbon and nitrogen elements, further manifesting that the nanoparticles are composed of nickel and phosphorus, which are uniformly anchored on $g-C_3N_4$ nanosheets. As illustrated in Fig. S6, the energy dispersive X-ray (EDX) spectra reveal the elemental composition of C, N, Ni and P in the hybrid

systems, and the atomic ratio of Ni: P is calculated to be approximately 2: 1 for the Ni_2P phase. In addition, the N_2 adsorption–desorption isotherms (Fig. S7) demonstrate the type IV hysteresis loops for both $g-C_3N_4$ and $g-C_3N_4$/3.5% Ni_2P, corroborating that the mesoporous feature of $g-C_3N_4$ can be retained even after incorporating Ni_2P nanoparticles. It is found that the Brunauer–Emmett–Teller (BET) surface area of $g-C_3N_4$/3.5% Ni_2P (57.73 m^2 g^{-1}) is much lower than that of pure $g-C_3N_4$ (85.01 m^2 g^{-1}), and the average pore size and pore volume of $g-C_3N_4$ are also marginally decreased, which can be ascribed to the partial filling and blocking of mesopores upon loading with Ni_2P.

Fig. 4 presents the X-ray diffraction (XRD) patterns of the pure Ni_2P, $g-C_3N_4$ and $g-C_3N_4$/Ni_2P hybrid photocatalysts. The pristine Ni_2P sample displays clear diffraction peaks at 40.7°, 44.6°, 47.3°, 54.2°, 55.0°, 66.4°, 72.7°, 74.8°, 80.2°, 80.9 ° and 88.8° corresponding to (111), (201), (210), (300), (211), (310), (311), (400), (302), (401) and (321) planes of the hexagonal phase structure of Ni_2P (JCPDS#74-1385), respectively. In addition, the strong and sharp diffraction peaks of the XRD pattern unveil the high crystallinity of Ni_2P, and no other crystalline impurities are detected, claiming that the pure phase Ni_2P is successfully synthesized by a two-step solvent-phase method. Both pure $g-C_3N_4$ and$g-C_3N_4$-based hybrid systems have two distinct diffraction peaks at 13.0° and 27.4° belonging to graphitic structure of $g-C_3N_4$ (JCPDS#87-1526), which can be well-indexed to the (100) plane with in-plane structural packing and (002) plane of interlayer stacking with conjugated aromatic systems, respectively [51]. Apart from that, no other crystalline structures are detected in the diffraction patterns, ascertaining the successful formation of $g-C_3N_4$/Ni_2P hybrid nanostructures. Furthermore, the intensities of (111), (201), (210) and (300) diffraction peaks of Ni_2P gradually enhance with an increase in the contents of Ni_2P in the hybrid heterojunction samples. It is discernible that no noticeable change is observed for the diffraction peaks of Ni_2P and $g-C_3N_4$ in the hybrid systems, signifying that incorporating Ni_2P into $g-C_3N_4$ by the solution-phase method does not conceivably alter the crystal structure of both $g-C_3N_4$ and Ni_2P components.

The Fourier transform infrared (FTIR) spectra of pure $g-C_3N_4$ and $g-C_3N_4$/Ni_2P hybrid photocatalysts are delineated in Fig. S8. The broad absorption band ranging from 3100 to 3300 cm^{-1} can be accredited to the stretching modes of secondary and primary amines and their intermolecular hydrogen-bonding interactions [52,53]. The band at approximately 810 cm^{-1} belongs to the characteristic breathing mode of tri-*s*-triazine units [53,54], whereas a broad adsorption band in the range of 1200–1800 cm^{-1} is assigned to the skeletal vibrations of the heptazine heterocyclic ring units [30,55–57]. From the FTIR spectra results, pure $g-C_3N_4$ and $g-C_3N_4$/Ni_2P hybrid photocatalysts possess similar absorption bands, elucidating that there is no variation in the stretching and bending vibrations of $g-C_3N_4$ after the incorporation of Ni_2P nanoparticles.

The surface chemical states of $g-C_3N_4$/10% Ni_2P and $g-C_3N_4$/3.5% Ni_2P were analyzed by X-ray photoelectron spectroscopy (XPS). As shown in Fig. S9 and S10, the N 1 s and C 1 s XPS spectra exemplify the characteristic nature of $g-C_3N_4$ [43]. The Ni $2p_{3/2}$ spectrum shows three peaks at 852.8, 856.5 and 862.1 eV, which can be assigned to the $Ni^{\delta+}$ oxidation state in Ni_2P, the oxidized Ni species (Ni^{2+}) and the satellite of the Ni $2p_{3/2}$ peak, respectively. Moreover, three peaks are observed at 870.2, 875.1 and 880.6 eV for the Ni $2p_{1/2}$ energy level, which are originated from $Ni^{\delta+}$ in Ni_2P, Ni^{2+} formed by the surface oxidation and the satellite of Ni $2p_{1/2}$ peak, respectively. Meanwhile, the P 2p spectrum (Fig. S9d) manifests the binding energies at 129.2 and 133.2 eV, which are ascribed to the $P^{\delta-}$ of Ni_2P and the surface nickel phosphate species, correspondingly. It is worth noting that the P signals of the $g-C_3N_4$/3.5% Ni_2P sample are weak due to the low Ni_2P content deposited and embedded by $g-C_3N_4$. Nonetheless, the obtained Ni 2p and P 2p XPS spectra are in concord with previous literature reports [58,59], further accentuating the successful formation of Ni_2P in the $g-C_3N_4$ hybrid system.

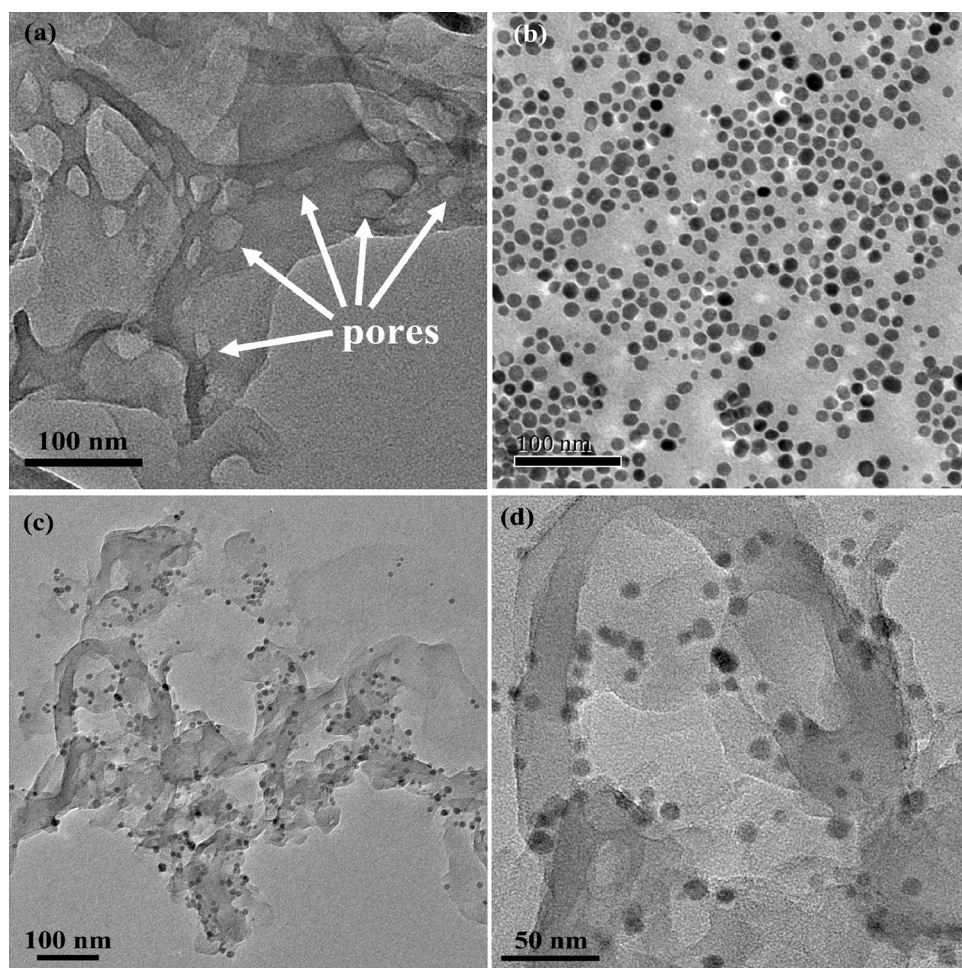The optical properties and charge carrier dynamics of the as-

Fig. 2. (a), (b) TEM images of pure g-C$_3$N$_4$ and Ni$_2$P nanoparticles, respectively. (c), (d) Low-magnification and high-magnification TEM images of g-C$_3$N$_4$/10% Ni$_2$P, respectively.

prepared photocatalysts were analyzed by ultraviolet-visible (UV-vis) and photoluminescence (PL) measurements. Fig. 5a shows the UV−vis diffuse reflectance spectra of pure g-C$_3$N$_4$, g-C$_3$N$_4$/Ni$_2$P and pure Ni$_2$P samples. Pure Ni$_2$P sample has a high absorption in the UV–vis region. The absorption edge of pure g-C$_3$N$_4$ and g-C$_3$N$_4$/Ni$_2$P is *ca.* 455 nm, which corresponds to a band gap of 2.73 eV, implying that the heterojunction nanocomposites retain the intrinsic band gap of g-C$_3$N$_4$. Furthermore, compared to pure g-C$_3$N$_4$, all the g-C$_3$N$_4$/Ni$_2$P samples display apparently enhanced intensity in the visible-light absorption with increasing Ni$_2$P amounts. This can be ascribed to the intrinsic absorption of black-colored Ni$_2$P nanoparticles. Fig. 5b presents the PL spectra of pure g-C$_3$N$_4$ and g-C$_3$N$_4$/Ni$_2$P with an excitation wavelength of 325 nm. The main emission peak for pure g-C$_3$N$_4$ and g-C$_3$N$_4$/Ni$_2$P samples is centered at *ca.* 460 nm, which corresponds well to the band gap energy. In contrast with pure g-C$_3$N$_4$, the PL intensities of g-C$_3$N$_4$/Ni$_2$P are overwhelmingly decreased, which stemmed from the rapid transfer of photoinduced electrons from g-C$_3$N$_4$ to Ni$_2$P through the intimate heterojunction interface, giving rise to the PL quenching and inhibition of electron–hole recombination.

The photocatalytic H$_2$ production activity over pure g-C$_3$N$_4$ and g-C$_3$N$_4$/Ni$_2$P heterojunction nanocomposites was evaluated under visible light irradiation (λ > 420 nm). As displayed in Fig. 6a, the photocatalytic rate of H$_2$ production of pure g-C$_3$N$_4$ is negligible due to the rapid recombination of photogenerated electron–hole pairs. It is also noteworthy that no H$_2$ was detected using bare Ni$_2$P. Surprisingly, incorporating g-C$_3$N$_4$ with a small amount of Ni$_2$P nanoparticles can substantially ameliorate the H$_2$ production activity. The optimal photocatalytic activity was achieved at 3.5 wt% of Ni$_2$P content with the corresponding H$_2$ evolution rate of 474.7 μmol h^{-1} g^{-1}. At higher

amounts of Ni$_2$P (*i.e.* 5, 7.5 and 10 wt%), the rate of H$_2$ evolution was profoundly decreased. This phenomenon is caused by the shielding effect of the light absorption as a result of excessive Ni$_2$P nanoparticles in the hybrid photocatalysts [40,60]. Fig. 6b shows the stability of photocatalytic H$_2$ evolution using the g-C$_3$N$_4$/3.5% Ni$_2$P catalyst as the representative sample. There is no obvious decrease in the H$_2$ evolution rate after five successive runs within 20 h of photocatalytic reaction, revealing the superior long-term stability of g-C$_3$N$_4$/Ni$_2$P heterojunction nanocomposites. Moreover, the apparent quantum yield (AQY) value of g-C$_3$N$_4$/3.5% Ni$_2$P was estimated to be 3.2% at 435 nm. To our knowledge, it is worth highlighting that our AQY value and H$_2$ production rate obtained herein are indeed higher than those in other g-C$_3$N$_4$ hybrid systems loaded with noble-metal-free co-catalysts based on the literature reports (Table S1) [15,25,29,45,47]. Notably, the structure and morphology of the spent g-C$_3$N$_4$/3.5% Ni$_2$P hybrid nanocomposites basically remain unchanged as evidenced by the TEM and XRD analyses (Fig. S11 and S12), indicating that the heterojunction nanocomposites are highly stable under prolonged visible light irradiation.

Time-resolved PL (TRPL) spectroscopy was employed to characterize the lifetime of charge carriers (Fig. 7a). The fluorescence decay curves were fitted based on the bi-exponential kinetic function: $I(t) = A_1\exp(-t/\tau_1) + A_2\exp(-t/\tau_2)$ [61], where τ_1 and τ_2 are the emission lifetimes, and A_1 and A_2 are the corresponding amplitudes. The detailed kinetic parameters for pure g-C$_3$N$_4$ and g-C$_3$N$_4$/3.5% Ni$_2$P are summarized in Table S2. The individual lifetime components (τ_1 and τ_2) of g-C$_3$N$_4$/3.5% Ni$_2$P hybrid photocatalysts are shorter than that of the pure g-C$_3$N$_4$. In order to relate the overall emission decay behaviors, the average lifetime (τ_{ave}) was evaluated using the following
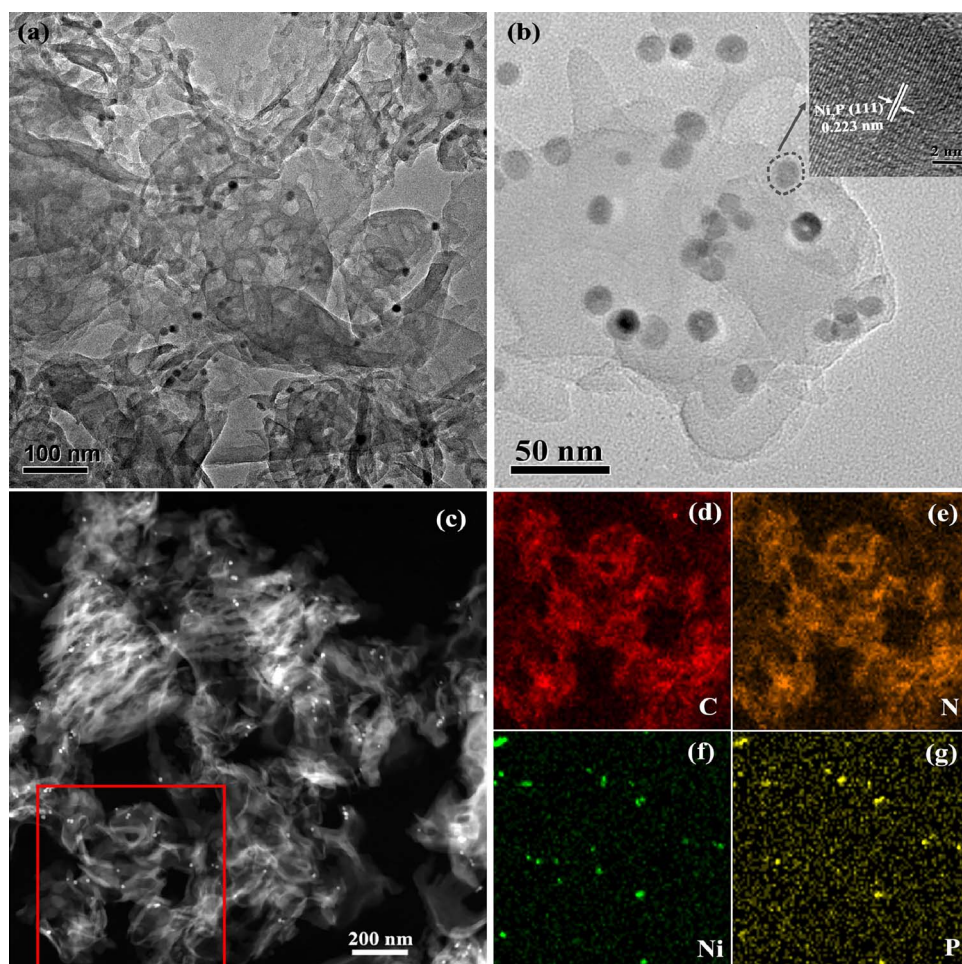
Fig. 3. Structural characterization of g-C$_3$N$_4$/3.5% Ni$_2$P. (a) Low-magnification TEM image. (b) High-magnification TEM image along with HRTEM image (inset). (c) HAADF image. (d)–(g) STEM elemental mapping of C, N, Ni and P, respectively, of the indicated red square area in the HAADF image (c). (For interpretation of the references to colour in this figure legend, the reader is referred to the web version of this article.)
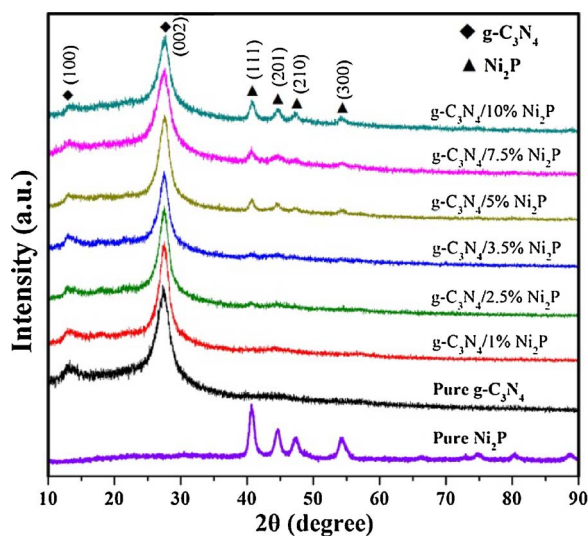

Fig. 4. XRD patterns of pure Ni$_2$P, pure g-C$_3$N$_4$ and g-C$_3$N$_4$/Ni$_2$P hybrid photocatalysts with different Ni$_2$P amounts.

equation: $\tau_{ave} = (A_1\tau_1{}^2 + A_2\tau_2{}^2)/(A_1\tau_1 + A_2\tau_2)$ [62]. It can be clearly deduced that after incorporating with an optimal concentration of Ni$_2$P (*i.e.* 3.5 wt%), the average emission lifetime of g-C$_3$N$_4$ is shortened from 6.46 to 5.58 ns. The decreased emission lifetime of g-C$_3$N$_4$/3.5% Ni$_2$P signifies the rapid interfacial electron injection from g-C$_3$N$_4$ to Ni$_2$P across the heterojunction interface. As such, this is attributed to the emergence of non-radiative quenching routes and importantly, the

TRPL results are in accordance with our steady-state PL quenching measurements. The electronic band structures of the pure g-C$_3$N$_4$ and g-C$_3$N$_4$/3.5% Ni$_2$P heterojunction nanocomposites were determined by the electron paramagnetic resonance (EPR) analysis at room temperature (Fig. 7b). For both pure g-C$_3$N$_4$ and g-C$_3$N$_4$/3.5% Ni$_2$P samples, a single Lorentzian line centered at 3508 G with a g value of 2.0045 is displayed. The Lorentzian line is attributed to an unpaired electron on the carbon atoms of the π-conjugated aromatic rings of g-C$_3$N$_4$ [63–65]. The intensity of the EPR signal of the g-C$_3$N$_4$/3.5% Ni$_2$P sample increases significantly in contrast with pure g-C$_3$N$_4$, which accounts for a higher concentration of lone electron pairs and improved charge delocalization present in the hybrid g-C$_3$N$_4$/3.5% Ni$_2$P sample. This in turn leads to a greater density of charge carriers when incorporating with Ni$_2$P, which is eminently beneficial to the photocatalytic process [66–68].

Apart from the photocatalytic H$_2$ production experiments, photoelectrochemical (PEC) analysis was performed to gain more insights into the rational significance of interfacial interactions and charge transfer phenomena over the g-C$_3$N$_4$/Ni$_2$P heterojunction systems. Fig. 7c manifests the transient photocurrent responses (I–t curves) for the pure g-C$_3$N$_4$ and g-C$_3$N$_4$/3.5% Ni$_2$P samples, with five on–off cycles of intermittent visible light irradiation (λ > 420 nm). Interestingly, the photocurrent intensity of g-C$_3$N$_4$/3.5% Ni$_2$P is considerably higher by three times than that of the parent g-C$_3$N$_4$ sample. Furthermore, the g-C$_3$N$_4$/3.5% Ni$_2$P sample endows a relatively stronger photoresponse with varying potentials compared to pure g-C$_3$N$_4$ as ascertained by the linear sweep voltammetry (LSV) curves (Fig. S13). To further confirm the enhanced charge separation efficiency, the electrochemical impedance spectroscopy (EIS) Nyquist plots of pure g-C$_3$N$_4$ and g-C$_3$N$_4$/
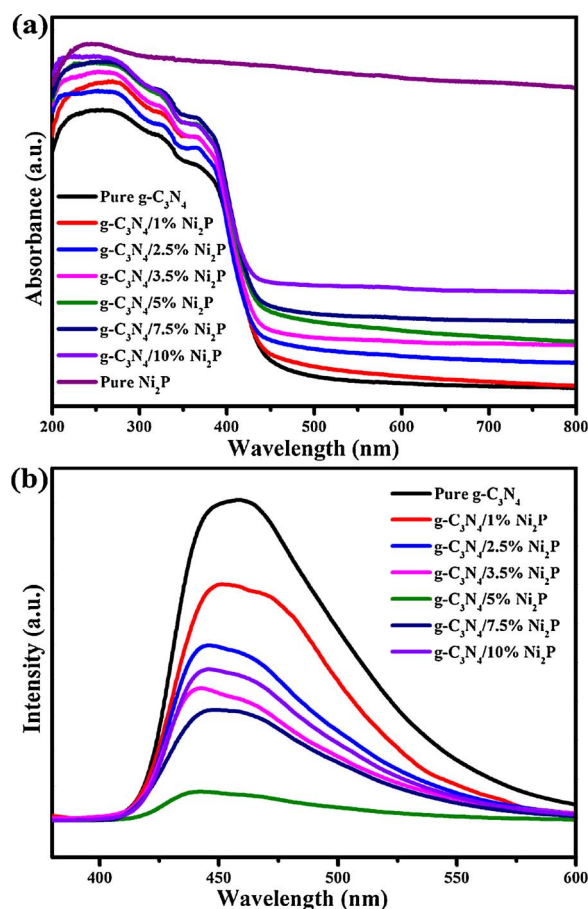
Fig. 5. (a) UV–vis diffuse reflectance spectra of pure g-C$_3$N$_4$, g-C$_3$N$_4$/Ni$_2$P and pure Ni$_2$P samples. (b) PL spectra of pure g-C$_3$N$_4$ and g-C$_3$N$_4$/Ni$_2$P heterojunction nanocomposites.
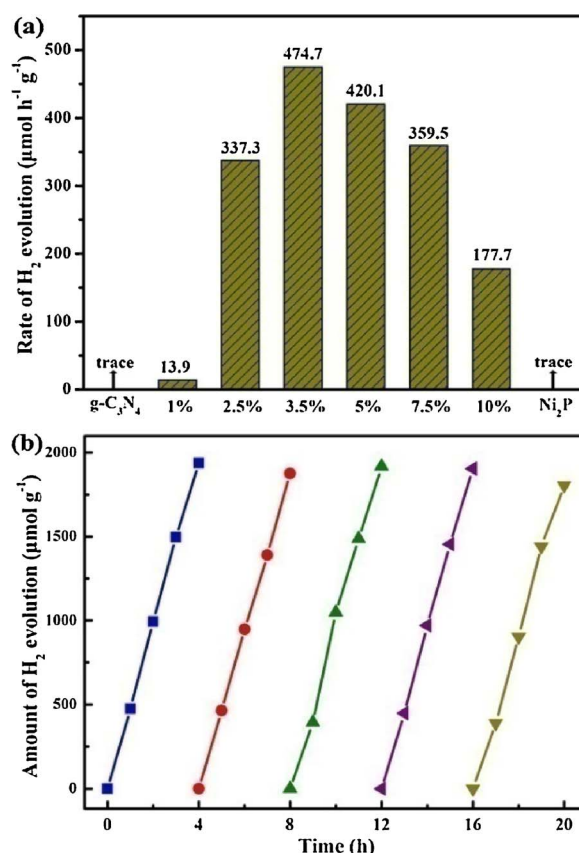

Fig. 6. (a) Photocatalytic H$_2$ evolution rates over various samples under visible light irradiation ($\lambda > 420$ nm). (b) Recycle runs of H$_2$ evolution over the g-C$_3$N$_4$/3.5% Ni$_2$P sample.

3.5% Ni$_2$P electrodes were measured in the dark and under visible light irradiation ($\lambda > 420$ nm) using 0.1 M Na$_2$SO$_4$ aqueous solutions as the electrolyte (Fig. 7d). By comparing the EIS Nyquist plots of both samples under dark and visible light irradiation, it is clearly observed that the arc radii of the Nyquist plots under light illumination are smaller relative to those in the dark, indicating the prominent role of g-C$_3$N$_4$ as a light-harvesting nanomaterial in photocatalytic activities. In comparison with pure g-C$_3$N$_4$, the arc radius of the Nyquist plot for the g-C$_3$N$_4$/3.5% Ni$_2$P electrode becomes noticeably smaller under dark and visible light irradiation, further inferring the prevailing roles of loaded Ni$_2$P nanoparticles as the H$_2$ evolution cocatalysts which accelerate the charge transport and separation of g-C$_3$N$_4$. Such results elucidate that the heterojunction nanocomposite presents a lower charge transfer resistance and boosted electrical conductivity, thus facilitating effective interfacial electron transfer at the 0D-2D heterointerface between Ni$_2$P and g-C$_3$N$_4$. In this regard, the unprecedented H$_2$ evolution activity of the g-C$_3$N$_4$/Ni$_2$P nanohybrids was emerged from the exceptional Ni$_2$P reduction co-catalysts serving as electron reservoir and also active reaction sites.

On the basis of the above experimental results, a plausible reaction mechanism of photocatalytic H$_2$ production in the g-C$_3$N$_4$/Ni$_2$P hybridized system was proposed (Fig. 8). When g-C$_3$N$_4$ is irradiated by visible light, electrons are photoexcited into the conduction band (CB) and simultaneously, this leads to the generation of holes in the valence band (VB). In the absence of co-catalysts, there is a rapid recombination of the electrons from the CB and holes from the VB in the parent g-C$_3$N$_4$. Upon anchoring with Ni$_2$P nanoparticles, the photoinduced electron in the CB of g-C$_3$N$_4$ could rapidly transfer to the metallic Ni$_2$P through the heterostructured interfaces between g-C$_3$N$_4$ and Ni$_2$P. On the other hand, the photogenerated holes are quenched by TEOA. Therefore, the

recombination of electron–hole pairs is greatly retarded. The electrons trapped by the Ni$_2$P can catalyze the reduction of protons to H$_2$, giving rise to the efficient photocatalytic H$_2$ evolution from the H$_2$O reduction.

3. Conclusions

In short, we have successfully developed a facile route to synthesize 0D monodisperse Ni$_2$P nanoparticles with high-purity phase and well-crystallized. The obtained Ni$_2$P nanoparticles are firmly anchored onto the 2D porous g-C$_3$N$_4$ nanosheets through ultrasonication assisted by the solution-phase self-assembly method. The main highlight of this work lies in the concept of well-contacted 0D-2D heterojunction interfaces, in which Ni$_2$P acts as a low-cost co-catalyst conjugated with porous g-C$_3$N$_4$ for remarkably efficient noble-metal-free photocatalytic H$_2$ evolution under visible light irradiation. The highest H$_2$ evolution rate of 474.7 μmol h^{-1} g^{-1} with a corresponding AQY of 3.2% at 435 nm and excellent recycling stability have been attained in the optimized g-C$_3$N$_4$/3.5% Ni$_2$P hybrid photocatalysts. As a whole, the PEC, steady-state PL, TRPL and EPR studies reveal that Ni$_2$P co-catalysts serve as reactive activation sites for effectively promoting the charge separation and migration to suppress the electron-hole recombination, thus increasing the photocatalytic efficiency of H$_2$ production. All in all, this work not only provides a novel approach to integrate Ni$_2$P with g-C$_3$N$_4$ for the formation of intimate 0D-2D heterointerfaces, but also deepens the understanding of charge carrier dynamics in the heterojunction nanocomposites for artificial photosynthesis. As such, this opens up new opportunities and possibilities for engineering other g-C$_3$N$_4$-based hybrid nanostructures by incorporating a large array of nanocrystals for diversified technological applications in the solar energy conversion and environmental cleaning.
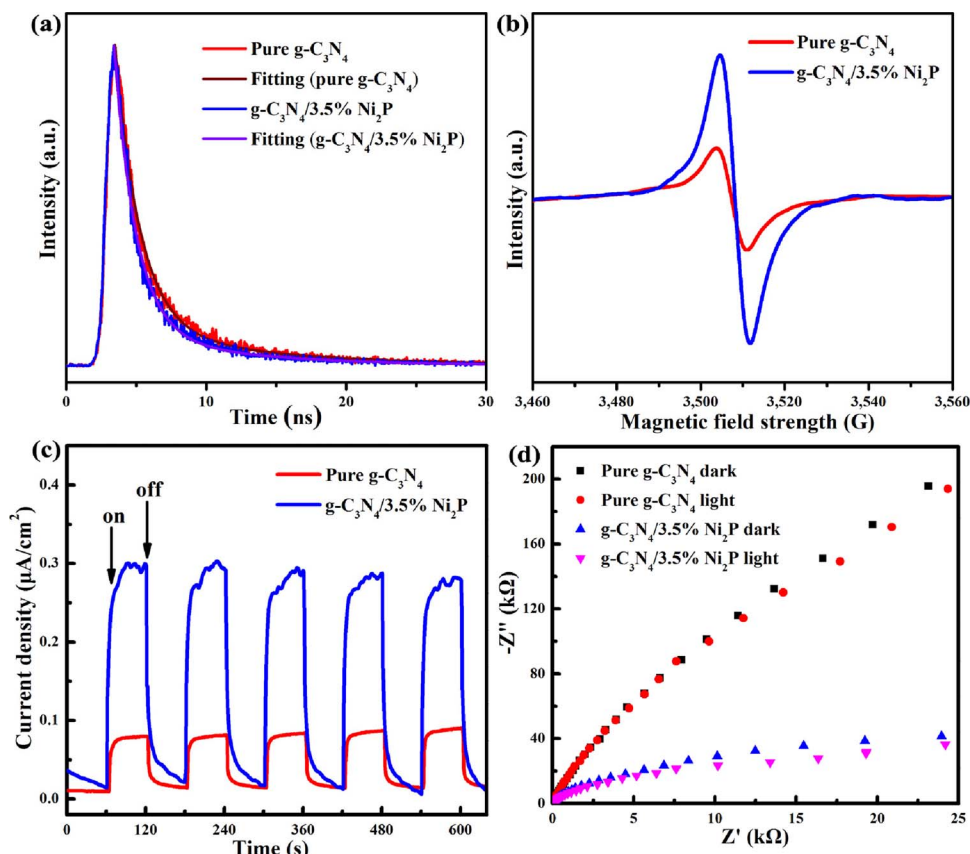
Fig. 7. TRPL decay curves (a) and EPR spectra (b) of pure g-C$_3$N$_4$ and g-C$_3$N$_4$/3.5% Ni$_2$P samples. Transient photocurrent response curves (c) and EIS Nyquist plots (d) of pure g-C$_3$N$_4$ and g-C$_3$N$_4$/3.5% Ni$_2$P in 0.1 M Na$_2$SO$_4$ solution under dark and visible light irradiation.
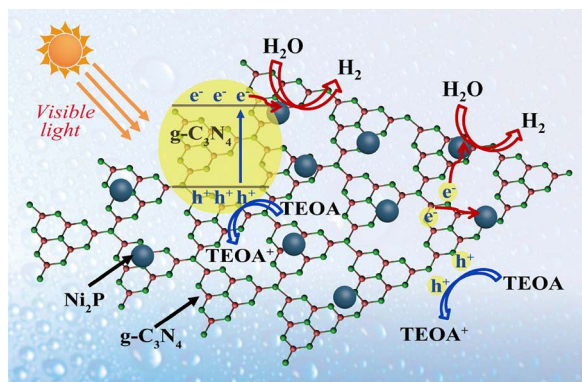

Fig. 8. Schematic of the charge separation and transfer in the photocatalytic H$_2$ evolution for the g-C$_3$N$_4$/Ni$_2$P heterojunction nanocomposites under visible light irradiation.

4. Experimental procedures

4.1. Catalyst synthesis

Synthesis of Ni$_2$P nanoparticles: In a typical synthesis, 1 mmol of Ni (acac)$_2$ and 7 mL of OAm were mixed together and stirred magnetically at 60 °C for 10 min under a high-purity argon gas. After that, 2 mmol of TOP (0.88 mL) was quickly injected into the solution, followed by re-setting the temperature up to 120 °C and kept at this temperature for 10 min. Next, the solution was raised to 210 °C for 30 min. Then the reaction mixture was cooled down to 80 °C, and 5 mmol of TOP (2.2 mL) was rapidly injected into the above hot solution. Subsequently, the mixture was heated up to 325 °C and maintained for 60 min before cooling down to room temperature. Finally, the black precipitate was washed several times with a mixture of hexane and ethanol (1:3) by centrifugation (9000 rpm, 3 min), and then dried in vacuum at 60 °C

overnight.

Synthesis of g-C$_3$N$_4$/Ni$_2$P heterojunction nanostructures: Firstly, porous g-C$_3$N$_4$ has been synthesized by the thermal polycondensation of urea according to our previous reported procedures [64]. A solution-phase method was employed to incorporate Ni$_2$P nanoparticles onto porous g-C$_3$N$_4$ nanosheets by means of mixing two immiscible solutions (Ni$_2$P in hexane and g-C$_3$N$_4$ in DMF) *via* constant sonication. This process is favorable to maintain the desired size and morphology of Ni$_2$P nanoparticles even after hybridizing with g-C$_3$N$_4$. Briefly, 160 mg of g-C$_3$N$_4$ sample was dispersed in 20 mL of DMF and continuously sonicated for 30 min. Then, a varied amount of well-dispersed Ni$_2$P in hexane was added dropwise into the above suspension under sonication, followed by performing ultra-sonication for the additional 60 min to ensure the proper dispersion of the g-C$_3$N$_4$/Ni$_2$P in DMF/hexane mixture. After that, 10 mL of ethanol was added into the mixture and sonicated for 20 min before the product was separated from the mixture *via* centrifugation (10000 rpm, 5 min). Following that, the product underwent ultra-sonication in 35 mL of toluene for 60 min, and then the suspension was aged for 24 h at room temperature. Thereafter, by carefully removing and discarding the supernatant, the resulting pre-cipitate was separated by centrifugation and washed with excessive ethanol for three times before it was placed in a vacuum oven at 120 °C for 8 h to remove the residual solvents prior to the materials char-acterization.

4.2. Materials characterization

Transmission electron microscopy (TEM) images, selected area electron diffraction (SAED) patterns, high-angle annular dark field scanning transmission electron microscopy (HAADF-STEM), energy dispersive X-ray spectroscopy (EDX) and TEM-EDX elemental mapping were obtained with a TECNAI F-30 transmission electron microscope operating at 300 kV. Powder X-ray diffraction (XRD) data were

determined by a Bruker D8-Advance X-ray powder diffractometer with Cu Kα radiation. Ultraviolet-visible (UV-vis) absorption spectra were measured by using a Cary 5000 UV–vis spectrometer (Varian). The photoluminescence (PL) and fluorescence decay spectra were acquired on a FLS980 spectrophotometer (Edinburgh Instruments). Fourier transform infrared (FTIR) spectra were recorded with a Nicolet Nexus-670 FT-IR spectrometer. X-ray photoelectron spectroscopy (XPS) measurements were performed by a VG ESCALAB 220i-XL system. Electron paramagnetic resonance (EPR) measurements were carried out by using a Bruker EMX 10/12 X-band EPR spectrometer. N_2 adsorption−desorption plots were collected from a TriStar 3020 system.

4.3. Photocatalytic hydrogen production

The photocatalytic hydrogen production experiments were performed in a closed and connected vacuum circulatory system using a Pyrex flask (total volume of 250 mL with a top irradiation area of around 19.6 cm^2). The as-developed g-C$_3$N$_4$/Ni$_2$P photocatalyst (50 mg) was dispersed in the reactor containing a mixed solution of 10 mL of TEOA and 100 mL of distilled water. Prior to light irradiation, the suspension was sonicated for 5 min, subsequently degassed by evacuating the reactor followed by purging with argon. Afterwards, a circular cooling water system was turned on and the reactor was vertically irradiated by a 300 W high-pressure Xe lamp (CEL-HXUV300, Beijing Aulight Co., Ltd.) with a UV-cutoff filter (λ > 420 nm) under magnetic stirring. The amount of hydrogen evolved was analyzed using a gas chromatography system (Techcomp GC-7900, Ar as the carrier gas, a 5 Å molecular sieve column, a thermal conductivity detector (TCD)). The apparent quantum yield (AQY) was defined by the following equation and was measured under the same conditions of the reaction except by utilizing a 435 nm band pass filter with full width at half maximum (FWHM) of 10 nm.

$$AQY(\%) = \frac{\text{the number of reacted electrons}}{\text{the number of incident photons}} \times 100$$
$$= \frac{\text{the number of evolved } H_2 \text{ molecules} \times 2}{\text{the number of incident photons}} \times 100$$

4.4. Photoelectrochemical (PEC) measurements

The photoelectrochemical (PEC) measurements were conducted using a VSP-300 (Biologic) potentiostat *via* a standard three-electrode system under visible light irradiation with a 420 nm cutoff filter through a 300 W Xe lamp (CEL-HXUV300, Beijing Aulight Co., Ltd.). The working electrodes were prepared as follows: 6 mg of photocatalyst powder was added into 3 mL of ethanol and the dispersion was then ultrasonicated for 10 min. The prepared slurry was deposited and distributed uniformly across the 1 cm × 2 cm carbon fiber paper, which served as an underlying substrate of the working electrode. Lastly, the carbon fiber paper was dried in an oven at 120 °C for 3 h under vacuum to increase the adhesion of the sample onto the carbon fiber. Meanwhile, a saturated Ag/AgCl electrode, a piece of Pt sheet, and 0.1 M of Na$_2$SO$_4$ were used as a reference electrode, a counter electrode, and electrolyte. The transient photocurrent response results were measured with the lamp on and off at a fixed time interval of 60 s under a constant applied bias of 0.5 V. Electrochemical impedance spectroscopy (EIS) spectra were measured over a frequency range of 10^{-1} to 10^5 Hz at an applied potential of 0.5 V vs. Ag/AgCl with an alternating current perturbation signal of 0.01 V in the dark and under visible light irradiation (λ > 420 nm). Additionally, the photocurrent response was obtained by linear sweep voltammetry (LSV) in dark and under visible light irradiation (λ > 420 nm) over the potential range of −0.6 to 0.3 V.

Appendix A. Supplementary data

Supplementary data associated with this article can be found, in the online version, at http://dx.doi.org/10.1016/j.apcatb.2017.08.041.

References

[1] W.-J. Ong, L.L. Tan, S.P. Chai, S.T. Yong, A.R. Mohamed, ChemSusChem 7 (2014) 690–719.
[2] Y.F. Zhao, X.D. Jia, G.I.N. Waterhouse, L.Z. Wu, C.H. Tung, D. O'Hare, T.R. Zhang, Adv. Energy Mater. 6 (2016) 1501974.
[3] W.-J. Ong, L.L. Tan, Y.H. Ng, S.T. Yong, S.P. Chai, Chem. Rev. 116 (2016) 7159–7329.
[4] D. Masih, Y. Ma, S. Rohani, Appl. Catal. B Environ. 206 (2017) 556–588.
[5] G.G. Zhang, Z.-A. Lan, L.H. Lin, S. Lin, X.C. Wang, Chem. Sci. 7 (2016) 3062–3066.
[6] L. Zhou, H. Zhang, H. Sun, S. Liu, M.O. Tade, S. Wang, W. Jin, Catal. Sci. Technol. 6 (2016) 7002–7023.
[7] S. Cao, J. Yu, J. Phys. Chem. Lett. 5 (2014) 2101–2107.
[8] H.J. Yu, R. Shi, Y.X. Zhao, T. Bian, Y.F. Zhao, C. Zhou, G.I.N. Waterhouse, L.Z. Wu, C.H. Tung, T.R. Zhang, Adv. Mater. 29 (2017) 1605148.
[9] X.P. Liu, H. Qin, W.L. Fan, Sci. Bull. 61 (2016) 645–655.
[10] Y. Wang, X.C. Wang, M. Antonietti, Angew. Chem. Int. Ed. 51 (2012) 68–89.
[11] Y. Zheng, J. Liu, J. Liang, M. Jaroniec, S.Z. Qiao, Energy Environ. Sci. 5 (2012) 6717–6731.
[12] W.-J. Ong, L.L. Tan, S.P. Chai, S.T. Yong, A.R. Mohamed, Nano Energy 13 (2015) 757–770.
[13] S. Yang, Y. Gong, J. Zhang, L. Zhan, L. Ma, Z. Fang, R. Vajtai, X. Wang, P.M. Ajayan, Adv. Mater. 25 (2013) 2452–2456.
[14] M. Zhang, X. Wang, Energy Environ. Sci. 7 (2014) 1902–1906.
[15] J. Wen, J. Xie, X. Chen, X. Li, Appl. Surf. Sci. 391 (2017) 72–123 (Part B).
[16] J. Chen, D.M. Zhao, Z.D. Diao, M. Wang, S.H. Shen, Sci. Bull. 61 (2016) 292–301.
[17] A. Indra, P.W. Menezes, K. Kailasam, D. Hollmann, M. Schrçder, A. Thomas, A. Brueckner, M. Driess, Chem. Commun. 52 (2016) 104–107.
[18] S. Martha, A. Nashim, K.M. Parida, J. Mater. Chem. A 1 (2013) 7816–7824.
[19] Z. Tong, D. Yang, Z. Li, Y. Nan, F. Ding, Y. Shen, Z. Jiang, ACS Nano 11 (2017) 1103–1112.
[20] F. Fina, H. Menard, J.T.S. Irvine, Phys. Chem. Chem. Phys. 17 (2015) 13929–13936.
[21] X. Wang, K. Maeda, A. Thomas, K. Takanabe, G. Xin, J.M. Carlsson, K. Domen, M. Antonietti, Nat. Mater. 8 (2009) 76–80.
[22] J.H. Sun, J.S. Zhang, M.W. Zhang, M. Antonietti, X.Z. Fu, X.C. Wang, Nat. Commun. 3 (2012) 1139.
[23] Q. Han, B. Wang, Y. Zhao, C. Hu, L. Qu, Angew. Chem. Int. Ed. 54 (2015) 11433–11437.
[24] Y. Hou, A.B. Laursen, J. Zhang, G. Zhang, Y. Zhu, X. Wang, S. Dahl, I. Chorkendorff, Angew. Chem. Int. Ed. 52 (2013) 3621–3625.
[25] H. Zhao, Y. Dong, P. Jiang, H. Miao, G. Wang, J. Zhang, J. Mater. Chem. A 3 (2015) 7375–7381.
[26] M.S. Akple, J. Low, S. Wageh, A.A. Al-Ghamdi, J. Yu, J. Zhang, Appl. Surf. Sci. A 358 (2015) 196–203 (Part A).
[27] J. Hong, Y. Wang, Y. Wang, W. Zhang, R. Xu, ChemSusChem 6 (2013) 2263–2268.
[28] Z.H. Chen, P. Sun, B. Fang, Z.G. Zhang, X.M. Fang, J. Phys. Chem. C 118 (2014) 7801–7807.
[29] J. Yu, S. Wang, B. Cheng, Z. Lin, F. Huang, Catal. Sci. Technol. 3 (2013) 1782–1789.
[30] L. Kong, Y. Dong, P. Jiang, G. Wang, H. Zhang, N. Zhao, J. Mater. Chem. A 4 (2016) 9998–10007.
[31] L. Bi, D. Meng, Q. Bu, Y. Lin, D. Wang, T. Xie, Phys. Chem. Chem. Phys. 18 (2016) 31534–31541.
[32] W. Cui, Q. Liu, Z. Xing, A.M. Asiri, K.A. Alamry, X. Sun, Appl. Catal. B Environ. 164 (2015) 144–150.
[33] Y.-H. Chung, K. Gupta, J.-H. Jang, H.S. Park, I. Jang, J.H. Jang, Y.-K. Lee, S.-C. Lee, S.J. Yoo, Nano Energy 26 (2016) 496–503.
[34] Y. Shi, B. Zhang, Chem. Soc. Rev. 45 (2016) 1529–1541.
[35] S. Cao, Y. Chen, C.-J. Wang, P. He, W.-F. Fu, Chem. Commun. 50 (2014) 10427–10429.
[36] Z. Sun, H. Zheng, J. Li, P. Du, Energy Environ. Sci. 8 (2015) 2668–2676.
[37] Q. Yue, Q. Wan, Z. Sun, X. Wu, Y. Yuan, P. Du, J. Mater. Chem. A 3 (2015) 16941–16947.
[38] Y. Dong, L. Kong, G. Wang, P. Jiang, N. Zhao, H. Zhang, Appl. Catal. B Environ. 211 (2017) 245–251.
[39] S. Cao, Y. Chen, C.-J. Wang, X.-J. Lv, W.-F. Fu, Chem. Commun. 51 (2015) 8708–8711.
[40] C. Li, Y. Du, D. Wang, S. Yin, W. Tu, Z. Chen, M. Kraft, G. Chen, R. Xu, Adv. Funct. Mater. 27 (2017) 1604328.

[41] S.-S. Yi, J.-M. Yan, B.-R. Wulan, S.-J. Li, K.-H. Liu, Q. Jiang, Appl. Catal. B Environ. 200 (2017) 477–483.
[42] H. Zhao, P. Jiang, W. Cai, Chem. Asian J. 12 (2017) 361–365.
[43] J. Wen, J. Xie, R. Shen, X. Li, X.Y. Luo, H. Zhang, A. Zhang, G. Bi, Dalton Trans. 46 (2017) 1794–1802.
[44] A. Indra, A. Acharjya, P.W. Menezes, C. Merschjann, D. Hollmann, M. Schwarze, M. Aktas, A. Friedrich, S. Lochbrunner, A. Thomas, M. Driess, Angew. Chem. 129 (2017) 1675–1679.
[45] Y. Chen, Z. Qin, Catal. Sci. Technol. 6 (2016) 8212–8221.
[46] H. Zhao, S. Sun, P. Jiang, Z.J. Xu, J Chem Eng, 315 (2017) 296–303.
[47] P. Ye, X. Liu, J. Locozzia, Y. Yuan, L. Gu, G. Xu, Z. Lin, J. Mater. Chem. A 5 (2017) 8493–8498.
[48] M. Li, Y. Chen, N. Ji, D. Zeng, D.-L. Peng, Mater. Chem. Phys. 147 (2014) 604–610.
[49] S. Guo, S. Sun, J. Am. Chem. Soc. 134 (2012) 2492–2495.
[50] J. Du, C. Chen, F. Cheng, J. Chen, Inorg. Chem. 54 (2015) 5467–5474.
[51] M.K. Bhunia, K. Yamauchi, K. Takanabe, Angew. Chem. Int. Ed. 126 (2014) 11181–11185.
[52] B.V. Lotsch, W. Schnick, Chem. Mater. 18 (2006) 1891–1900.
[53] Y. Cui, Z. Ding, P. Liu, M. Antonietti, X. Fu, X. Wang, Phys. Chem. Chem. Phys. 14 (2012) 1455–1462.
[54] G.G. Zhang, M.W. Zhang, X.X. Ye, X.Q. Qiu, S. Lin, X.C. Wang, Adv. Mater. 26 (2014) 805–809.
[55] J.R. Holst, E.G. Gillan, J. Am. Chem. Soc. 130 (2008) 7373–7379.
[56] X. Bai, L. Wang, R. Zong, Y. Zhu, J. Phys. Chem. C 117 (2013) 9952–9961.
[57] F. Dong, L. Wu, Y.J. Sun, M. Fu, Z.B. Wu, S.C. Lee, J. Mater. Chem. 21 (2011) 15171–15174.
[58] Y. Pan, Y.R. Liu, J.C. Zhao, K. Yang, J.L. Liang, D.D. Liu, W.H. Hu, D.P. Liu, Y.Q. Liu, C.G. Liu, J. Mater. Chem. A 3 (2015) 1656–1665.
[59] L.A. Stern, L.G. Feng, F. Song, X.L. Hu, Energy Environ. Sci. 8 (2015) 2347–2351.
[60] Z. Sun, B. Lv, J. Li, M. Xiao, X. Wang, P. Wang, J. Mater. Chem. A 4 (2016) 1598–1602.
[61] X.T. Wang, C.H. Liow, A. Bisht, X.F. Liu, T.C. Sum, X.D. Chen, S.Z. Li, Adv. Mater. 27 (2015) 2207–2214.
[62] Y. Chen, Y. Pu, Y. Hsu, J. Phys. Chem. C 116 (2012) 2967–2975.
[63] G.G. Liu, G.X. Zhao, W. Zhou, Y.Y. Liu, H. Pang, H.B. Zhang, D. Hao, X.G. Meng, P. Li, T. Kako, J.H. Ye, Adv. Funct. Mater. 26 (2016) 6822–6829.
[64] W.-J. Ong, L.K. Putri, Y.-C. Tan, L.L. Tan, N. Li, Y.H. Ng, X. Wen, S.P. Chai, Nano Res. 10 (2017) 1673–1696.
[65] J.S. Zhang, G.G. Zhang, X.F. Chen, S. Lin, L. Mohlmann, G. Dolega, G. Lipner, M. Antonietti, S. Blechert, X.C. Wang, Angew. Chem. Int. Ed. 51 (2012) 3183–3187.
[66] H.Q. Li, Y.X. Liu, Y.M. Cui, W.B. Zhang, C. Fu, X.C. Wang, Appl. Catal. B Environ. 183 (2016) 426–432.
[67] D. Zeng, W.-J. Ong, H. Zheng, M. Wu, Y. Chen, D.-L. Peng, M. Han, J. Mater. Chem. A. 5 (2017) 16171–16178.
[68] Y.F. Li, R.X. Jin, Y. Xing, J.Q. Li, S.Y. Song, X.C. Liu, M. Li, R.C. Jin, Adv. Energy Mater. 6 (2016) 1601273.